

Site-selective nuclear magnetic relaxation time in a superconducting vortex state

Mitsuaki Takigawa, Masanori Ichioka and Kazushige Machida
Department of Physics, Okayama University, Okayama 700-8530, Japan
 (October 25, 2018)

The temperature and field dependences of the site-selective nuclear spin relaxation time T_1 around vortices are studied comparatively both for s -wave and d -wave superconductors, based on the microscopic Bogoliubov-de Gennes theory. Reflecting low energy electronic excitations associated with the vortex core, the site selective temperature dependences deviate from those of the zero-field case, and T_1 becomes faster with approaching the vortex core. In the core region, T_1^{-1} has a new peak below the superconducting transition temperature T_c . The field dependence of the overall $T_1(T)$ behaviors for s -wave and d -wave superconductors is investigated and analyzed in terms of the local density of states. The NMR study by the resonance field dependence may be a new method to probe the spatial resolved vortex core structure in various conventional and unconventional superconductors.

PACS numbers: 74.60.Ec, 74.25.Jb, 76.60.Pc

I. INTRODUCTION

Much attention has been focused on vortex matter physics both of high T_c cuprates and of conventional superconductors.^{1,2} There are several experimental methods to extract the vortex properties, ranging from thermodynamic measurements such as specific heat to various transport experiments such as thermal conductivity under field. We can divide them into two categories: One of the methods such as scanning tunneling microscopy (STM) probes the electronic structure of the vortex, namely, low-lying excitations around a core. The other method probes the magnetic field distribution in the vortex state, exemplified by small angle neutron diffraction, or muon spin resonance (μ SR) experiments. These two methods are complimentary to each other. We definitely need to increase the list of the method and further refine the theoretical analysis of experimental data to extract useful information about the vortex properties.

Among various experimental methods mentioned above the nuclear magnetic resonance (NMR) experiment³ is unique because it provides us two kinds of information. Namely, the nuclear resonance spectrum reflects the magnetic field distribution and the longitudinal relaxation time T_1 probes electronic excitations in the vortex state through its T -dependence. The NMR experiment has been playing a vital role in distinguishing between s -wave and d -wave pairing symmetries in this respect, i.e. via T -dependence of T_1 . The power law $T_1^{-1} \propto T^3$ (T^5) behavior is taken as definitive evidence for a line (point) node in the gap structure of unconventional superconductors. This conclusion comes from a simple power counting of the density of states (DOS) at the Fermi level as a function of the energy E : $N(E) \propto E$ (E^3) for a line (point) node in a bulk superconductor at zero field. However, actual NMR experiments are performed under applied fields in a mixed state. The contribution of the vortex core is inevitably included in their data.^{4,5} Usually, T_1 is measured by selecting the resonance frequency at a most intensive sig-

nal in the resonance spectrum. However, the resonance spectrum reflects information of internal magnetic field distribution of the vortex lattice^{6,7} as mentioned above. Thus, by choosing the resonance field, we can specify the spatial position to detect the NMR signal. The signal at the maximum (minimum) cutoff comes from the vortex center (the furthest) site. The signal at the logarithmic singularity of the resonance field comes from the saddle points in the field distribution. By studying the position dependence of T_1 around vortices through the resonance frequency dependence, we can clarify the detail of the vortex contribution in the NMR experiments. It helps us in the analysis of the standardized procedure extracting the gap symmetry.

Low-lying excitation spectra around a vortex are not fully understood both experimentally and theoretically. The related problems are as follows. In the s -wave superconductors, the effect of the quantized energy level will appear in the quasi-particle state.⁸⁻¹¹ In the d -wave case, the low energy state around the vortex core extends outside the core due to the node of the superconducting gap, and shows the \sqrt{H} -like DOS relation (H is an applied field).¹²⁻¹⁶ We also need to estimate the quasi-particle transfer between vortices (such as the path of the transfer and its amplitude) to study the dHvA oscillation or transport phenomena in the mixed state.^{13,17} The excitation around the core plays a fundamental role in determining physical properties of superconductors. Several recent theories based on the microscopic Bogoliubov-de Gennes (BdG) equation investigate electromagnetic properties of mixed state^{18,19} in connection with the low-lying vortex excitations.^{8,15,16,20-22} In high T_c cuprates, the existence or non-existence of localized core excitations in d -wave pairing case is actively debated. Theoretical study suggested the zero-energy peak in the d -wave case, instead of the quantized energy level in the s -wave case.¹⁴⁻¹⁶ On the contrary, the STM experiments reported quantized energy level with large gap in YBCO (Ref. 23) and also in BSCCO (Ref. 24), and no peak within the superconducting gap in BSCCO (Ref. 25). A part of reasons of

the debate is due to limited experimental methods which directly probe the spatially resolved core structure. So far, the STM was only a method to detect it as mentioned before. A large number of thermodynamic or transport measurements probe spatially averaged quantities.

Here we propose a novel spatially resolved means, that is, vortex imaging to see electronic excitations associated with a vortex core by using NMR, and demonstrate how the T -dependence of T_1 is site-sensitive. Through this analysis, we are able to produce a spatial image of the low-lying excitation spectrum around a core. A similar idea of the NMR imaging is actually tested experimentally in high T_c materials by Slichter's group^{26,27} and theoretically proposed,^{28,29} and also in spin-Peierls system CuGeO₃ by Horvatić.³⁰

In order to analyze the NMR data and propose suitable NMR experiments, we perform a model calculation of T_1 to demonstrate how careful NMR experiment is valuable. The other purpose of this paper is to warn a pitfall when obtaining the conclusion of the nodal gap structure from the T -dependence of T_1 by performing the saddle point NMR. The position dependence of the NMR signal in the s -wave case was theoretically studied under some approximations.^{9,31} Here, we calculate it microscopically from the wave functions obtained by self-consistently solving the BdG equation for the extended Hubbard model in the s - and d -wave cases.

After giving the formulation of the problem in Sec. II, we show the results of basic vortex properties in this formulation in order to yield a coherent physical picture and to facilitate the later understanding of our results in Sec. III. In next section the T -dependence of T_1 is analyzed both for s -wave and d -wave superconductors. The field-dependence of T_1 is calculated in Sec. V. The final section is devoted to conclusion and discussions.³²

II. FORMULATION

A. Bogoliubov-de Gennes equation on lattice

The BdG theory and its equation are one of the most fundamental frameworks in the theory of superconductivity.³³ In principle, the solution of BdG equation should give all static properties of a type II superconductor under an applied field, which we concern. Here we consider the BdG equation defined on a lattice instead of continuum space. The latter approach is useful when the order parameter is described by the s -wave symmetry, but difficult to treat non-local higher angular momentum states such as d -wave. In contrast the lattice BdG theory is relatively easy to treat such a case and suitable for treating the s -wave and d -wave cases on an equal footing.

In terms of the eigen-energy E_α and the wave functions $u_\alpha(\mathbf{r}_i)$, $v_\alpha(\mathbf{r}_i)$ at i -site, the BdG equation for the

extended Hubbard model defined on the two-dimensional square lattice is given by

$$\sum_j \begin{pmatrix} K_{i,j} & D_{i,j} \\ D_{i,j}^\dagger & -K_{i,j}^* \end{pmatrix} \begin{pmatrix} u_\alpha(\mathbf{r}_j) \\ v_\alpha(\mathbf{r}_j) \end{pmatrix} = E_\alpha \begin{pmatrix} u_\alpha(\mathbf{r}_i) \\ v_\alpha(\mathbf{r}_i) \end{pmatrix}, \quad (1)$$

where

$$K_{i,j} = -\tilde{t}_{i,j} - \delta_{i,j}\mu, \quad (2)$$

$$D_{i,j} = \delta_{i,j}U\Delta_{i,i} + \frac{1}{2}V_{i,j}\Delta_{i,j} \quad (3)$$

with

$$\tilde{t}_{i,j} = t_{i,j} \exp[i\frac{\pi}{\phi_0} \int_{\mathbf{r}_i}^{\mathbf{r}_j} \mathbf{A}(\mathbf{r}) \cdot d\mathbf{r}] \quad (4)$$

and the on-site interaction U , the chemical potential μ and the flux quantum ϕ_0 . The transfer integral $t_{i,j} = t$ and the nearest neighbor (NN) interaction $V_{i,j} = V$ for the NN site pair \mathbf{r}_i and \mathbf{r}_j , and otherwise $t_{i,j} = V_{i,j} = 0$. The vector potential $\mathbf{A}(\mathbf{r}) = \frac{1}{2}\mathbf{H} \times \mathbf{r}$ in the symmetric gauge. The self-consistent condition for the pair potential is

$$\Delta_{i,j} = -\frac{1}{2} \sum_\alpha u_\alpha(\mathbf{r}_i) v_\alpha^*(\mathbf{r}_j) \tanh(E_\alpha/2T). \quad (5)$$

This BdG equation is self-consistently solved by following the numerical method of Wang and MacDonald.¹⁵

In the following we examine comparatively the s -wave and d -wave symmetry cases. The s -wave pair potential is given by

$$\Delta_s(\mathbf{r}_i) = U\Delta_{i,i}. \quad (6)$$

The $d_{x^2-y^2}$ -wave pair potential is given by

$$\Delta_d(\mathbf{r}_i) = \frac{V}{4}(\Delta_{\hat{x},i} + \Delta_{-\hat{x},i} - \Delta_{\hat{y},i} - \Delta_{-\hat{y},i}) \quad (7)$$

with

$$\Delta_{\pm\hat{e},i} = \Delta_{i,i\pm\hat{e}} \exp[i\frac{\pi}{\phi_0} \int_{\mathbf{r}_i}^{(\mathbf{r}_i+\mathbf{r}_{i\pm\hat{e}})/2} \mathbf{A}(\mathbf{r}) \cdot d\mathbf{r}]. \quad (8)$$

We consider the square vortex lattice case where nearest neighbor vortex is located at the 45° direction from the a axis. This vortex lattice configuration is suggested for d -wave superconductors, or s -wave superconductors with fourfold symmetric Fermi surface.^{13,39,40} The unit cell in our calculation is the square area of N_r^2 sites where two vortices are accommodated. Then, the magnetic field is determined as

$$H = \frac{2\phi_0}{(cN_r)^2} \quad (9)$$

where c is the atomic lattice constant. For typical high T_c cuprates, $H_{N_r=30}$ corresponds to an order of 15 Tesla.

We consider the area of N_k^2 unit cells. By introducing the quasi-momentum of the magnetic Bloch state,

$$\mathbf{k} = \frac{2\pi}{cN_r N_k} (l_x, l_y), \quad (l_x, l_y = 1, \dots, N_k) \quad (10)$$

we set

$$u_\alpha(\mathbf{r}) = \tilde{u}_\alpha(\mathbf{r}) e^{i\mathbf{k} \cdot \mathbf{r}}, \quad v_\alpha(\mathbf{r}) = \tilde{v}_\alpha(\mathbf{r}) e^{i\mathbf{k} \cdot \mathbf{r}}. \quad (11)$$

We solve Eq. (1) within a unit cell under the given \mathbf{k} . Then, α is labeled by \mathbf{k} and the eigen-values obtained by this calculation within a unit cell.

B. Boundary condition

We impose the periodic boundary condition given by the symmetry for the translation

$$\mathbf{R} = m\mathbf{u}_1 + n\mathbf{u}_2 \quad (12)$$

with m and n being integers, and \mathbf{u}_1 and \mathbf{u}_2 are unit vectors of the vortex lattice, i.e.,

$$\tilde{u}_\alpha(\mathbf{r} + \mathbf{R}) = \tilde{u}_\alpha(\mathbf{r}) e^{i\chi(\mathbf{r}, \mathbf{R})/2}, \quad (13)$$

$$\tilde{v}_\alpha(\mathbf{r} + \mathbf{R}) = \tilde{v}_\alpha(\mathbf{r}) e^{-i\chi(\mathbf{r}, \mathbf{R})/2}. \quad (14)$$

Here,

$$\chi(\mathbf{r}, \mathbf{R}) = -\frac{2\pi}{\phi_0} \mathbf{A}(\mathbf{R}) \cdot \mathbf{r} - \pi mn + \frac{2\pi}{\phi_0} (\mathbf{H} \times \mathbf{r}_0) \cdot \mathbf{R} \quad (15)$$

in the symmetric gauge when the vortex center is located at

$$\mathbf{r} = \mathbf{r}_0 + \frac{1}{2}(\mathbf{u}_1 + \mathbf{u}_2). \quad (16)$$

The phase factor⁴¹ in Eq. (8) is needed to satisfy the translational relation

$$\Delta_d(\mathbf{r} + \mathbf{R}) = \Delta_d(\mathbf{r}) e^{i\chi(\mathbf{r}, \mathbf{R})}. \quad (17)$$

C. Thermal Green function

In order to calculate various physical quantities, we must construct the Green functions from E_α , $u_\alpha(\mathbf{r})$, $v_\alpha(\mathbf{r})$ defined as

$$\begin{aligned} \hat{g}(x, x') &\equiv \begin{pmatrix} g_{11}(x, x') & g_{12}(x, x') \\ g_{21}(x, x') & g_{22}(x, x') \end{pmatrix} \\ &\equiv \begin{pmatrix} -\langle T_\tau [\hat{\psi}_\uparrow(x) \hat{\psi}_\uparrow^\dagger(x')] \rangle & -\langle T_\tau [\hat{\psi}_\uparrow(x) \hat{\psi}_\downarrow(x')] \rangle \\ -\langle T_\tau [\hat{\psi}_\downarrow^\dagger(x) \hat{\psi}_\uparrow^\dagger(x')] \rangle & -\langle T_\tau [\hat{\psi}_\downarrow^\dagger(x) \hat{\psi}_\downarrow(x')] \rangle \end{pmatrix}. \end{aligned} \quad (18)$$

with $x \equiv (\mathbf{x}, \tau)$. After the Fourier transformation of τ as

$$\hat{g}(x, x') = T \sum_{\omega_n} e^{-i\omega_n(\tau - \tau')} \hat{g}(\mathbf{x}, \mathbf{x}', \omega_n), \quad (19)$$

the thermal Green functions with the Fermionic imaginary frequency $\omega_n = 2\pi T(n + \frac{1}{2})$ are written as

$$g_{11}(\mathbf{x}, \mathbf{x}', \omega_n) = \sum_{\alpha} \frac{u_\alpha(\mathbf{x}) u_\alpha^*(\mathbf{x}')}{i\omega_n - E_\alpha} \quad (20)$$

$$g_{12}(\mathbf{x}, \mathbf{x}', \omega_n) = \sum_{\alpha} \frac{u_\alpha(\mathbf{x}) v_\alpha^*(\mathbf{x}')}{i\omega_n - E_\alpha} \quad (21)$$

$$g_{21}(\mathbf{x}, \mathbf{x}', \omega_n) = \sum_{\alpha} \frac{v_\alpha(\mathbf{x}) u_\alpha^*(\mathbf{x}')}{i\omega_n - E_\alpha} \quad (22)$$

$$g_{22}(\mathbf{x}, \mathbf{x}', \omega_n) = \sum_{\alpha} \frac{v_\alpha(\mathbf{x}) v_\alpha^*(\mathbf{x}')}{i\omega_n - E_\alpha}. \quad (23)$$

The derivation of this form of the thermal Green functions is given in Appendix A.

D. Local density of states

To understand the behavior of the position-dependent $T_1(\mathbf{r})$, we also consider the local density of states (LDOS) at \mathbf{r} . This is evaluated by using the thermal Green functions as

$$N_\uparrow(E, \mathbf{r}) = -\frac{1}{\pi} \text{Im} g_{11}(\mathbf{r}, \mathbf{r}, i\omega \rightarrow E + i\eta) \quad (24)$$

for the up-spin electron contributions, and

$$N_\downarrow(E, \mathbf{r}) = \frac{1}{\pi} \text{Im} g_{22}(\mathbf{r}, \mathbf{r}, i\omega \rightarrow E + i\eta) \quad (25)$$

for the down-spin electron contributions. Then, the LDOS is given by

$$\begin{aligned} N(E, \mathbf{r}) &= N_\uparrow(E, \mathbf{r}) + N_\downarrow(E, \mathbf{r}) \\ &= \sum_{\alpha} \{ |u_\alpha(\mathbf{r})|^2 \delta(E - E_\alpha) + |v_\alpha(\mathbf{r})|^2 \delta(E + E_\alpha) \}. \end{aligned} \quad (26)$$

For finite temperatures, the δ -functions in eq. (26) are replaced by the derivative $f'(E)$ of the Fermi distribution function $f(E)$:

$$N(E, \mathbf{r}) = -\sum_{\alpha} [|u_\alpha(\mathbf{r})|^2 f'(E_\alpha - E) + |v_\alpha(\mathbf{r})|^2 f'(E_\alpha + E)]. \quad (27)$$

This finite temperature LDOS corresponds to the differential tunnel conductance of STM experiments.

E. Nuclear relaxation time

We now evaluate the spin-spin correlation function $\chi_{-,+}(\mathbf{r}, \mathbf{r}', i\Omega_n)$.³¹ Its derivation is given in Appendix B. We obtain the nuclear spin relaxation rate by using Eq. (B4),

$$\begin{aligned} R(\mathbf{r}, \mathbf{r}') &= \text{Im} \chi_{-,+}(\mathbf{r}, \mathbf{r}', i\Omega_n \rightarrow \Omega + i\eta) / (\Omega/T)|_{\Omega \rightarrow 0} \\ &= - \sum_{\alpha, \beta} u_{\alpha}(\mathbf{r}) u_{\beta}^*(\mathbf{r}) [u_{\alpha}(\mathbf{r}') u_{\beta}^*(\mathbf{r}') + v_{\alpha}(\mathbf{r}') v_{\beta}^*(\mathbf{r}')] \\ &\quad \times \pi T f'(E_{\alpha}) \delta(E_{\alpha} - E_{\beta}). \end{aligned} \quad (28)$$

We consider the case $\mathbf{r} = \mathbf{r}'$ by assuming that the nuclear relaxation event occurs locally such as in Cu-site of high T_c cuprates. Then, the \mathbf{r} -dependent relaxation time is given by

$$T_1(\mathbf{r}) = 1/R(\mathbf{r}, \mathbf{r}). \quad (29)$$

In Eq. (28), we use $\delta(x) = \pi^{-1} \text{Im}(x - i\eta)^{-1}$ to consider the discrete energy level of the finite size calculation. We typically use $\eta = 0.01t$.

F. Parameters used and site assignment

The following parameter values are chosen: The average electron density per site ~ 0.9 by adjusting appropriately the chemical potential value μ . We normalize all the energy scales by the transfer integral t . For the s -wave case $U = -2.32t$ and $V = 0$. The resulting order parameter $\Delta_0/t = 0.5$ at $T=0$ and $H=0$. For the d -wave case $U = 0$ and $V = -4.2t$. Then $\Delta_0/t = 1.0$. The vortex unit cell is shown in Fig.1, where the selective sites (V, A, B, C, and S-sites) to consider $N(E, \mathbf{r})$ and $T_1(\mathbf{r})$ are also indicated. The magnetic field H is denoted by the unit cell size N_r as H_{N_r} . Thus as N_r increases, H itself decreases.

III. BASIC VORTEX PROPERTIES

In order to facilitate the understanding of the $T_1(\mathbf{r})$ -behaviors in the later section, we show some of the basic properties of vortex lattice. The following results coincide basically with those in the previous our own calculations either in quasi-classical theory for the vortex lattice of s - and d -wave cases,^{13,14,34–37} and in BdG for isolated vortex of the s -wave case^{10,11} and also with the preceding work by Wang and MacDonald.¹⁸

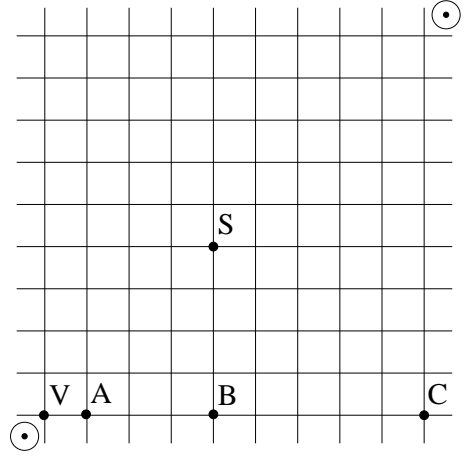


FIG. 1. A quarter region of the vortex unit cell which contains two vortices. Position of the sites V, A, B, C, and S in the square vortex lattice is indicated, where the nearest neighbor vortex is located in the 45° direction from the a -axis. The vortex center is shown by \odot . The solid lines show the square atomic lattice.

A. Order parameter profiles

The pair potential or the order parameter $\Delta(\mathbf{r})$ vanishes at the vortex center. $|\Delta(\mathbf{r})|$ exhibits the Friedel oscillations around the core both for the s -wave and d -wave cases whose period $\sim 1/k_F$ (k_F is the Fermi wave number). The amplitude of this quantum oscillation increases as the attractive interactions $|U|$ and $|V|$ become large because the quantum effects are enhanced when Δ_0/E_F increases (E_F is the Fermi energy). These characteristics coincide with those in the s -wave case in our previous study.¹⁰

As for the temperature dependence of the order parameter, the vortex core radius shrinks with decreasing T by the Kramer-Pesch effect.^{14,38} We confirm it for the d -wave case too. The shrinkage is saturated at a low temperature both in the s - and d -wave cases. There, the structure of $\Delta_s(\mathbf{r})$ and $\Delta_d(\mathbf{r})$ is almost independent of T . This is a quantum-limit effect which occurs for $T/T_c < \Delta_0/E_F$.¹⁰ We calculate the low temperature behavior of $T_1(\mathbf{r})$ by using the saturated pair potential. At higher temperatures, we calculate $T_1(\mathbf{r})$ by using the self-consistently obtained pair potential at each T .

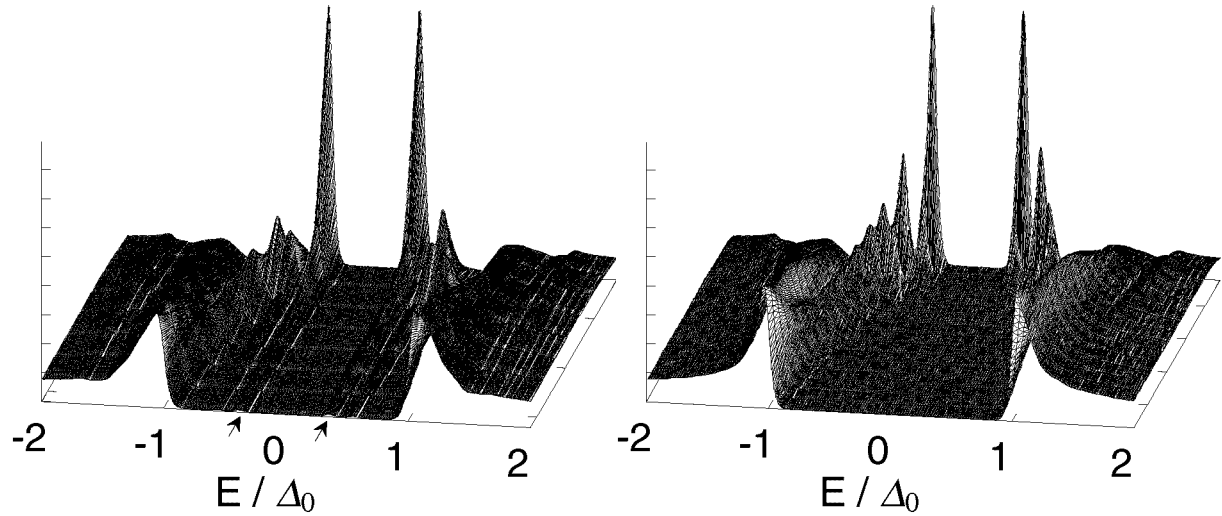


FIG. 2. (a) Local density of states $N(\mathbf{r}, E)$ for the s -wave case at $T = 0$ and H_{32} along the NN direction ($V \rightarrow S$). The backside (front) corresponds to V (S)-site defined in Fig. 1. (b) Local density of states $N(\mathbf{r}, E)$ along the NNN direction ($V \rightarrow C$). Note that the foot at the lowest levels at $E/\Delta_0 \sim \pm 0.28$ extends outward (arrows) along the NN direction.

B. Local density of states around a core

The LDOS is displayed as a function of the spatial position for the s -wave case in Fig. 2 and for the d -wave case in Fig. 3 at H_{32} . The spectral evolutions in Fig. 2 are shown for two different paths; along the nearest neighbor (NN) direction [Fig. 2(a)] and the next nearest neighbor (NNN) direction [Fig. 2(b)]. The low-lying excitations at the core, which correspond to the prominent peak structure, are characterized by the angular momentum (see for details Ref. 10). The higher and higher angular momentum states situated at the higher energy are activated successively when going outward, forming the

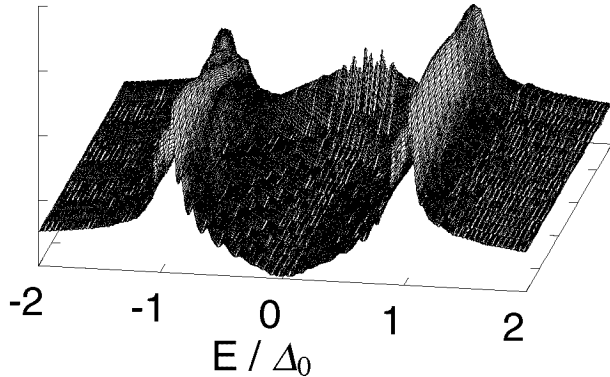


FIG. 3. Local density of states $N(\mathbf{r}, E)$ at $T = 0$ and H_{32} along the NNN direction ($V \rightarrow C$) for the d -wave case. The backside (front) corresponds to V (C)-site defined in Fig. 1. The spectral evolution along the NN direction, which is not shown, shows similar behavior to this figure.

characteristic spectral evolution in Fig. 2. The lowest excited state which is seen as the highest peak extends towards the NN direction rather than the NNN direction as indicated by arrows in Fig. 2(a).

The LDOS for the d -wave case is shown in Fig. 3. Since there is no discretized bound state around the core in this case, only the broad resonance peak centered at $E = 0$ is seen at the core, which evolves smoothly. At the farthest site the spectrum exhibits the known bulk behavior expected in the d -wave superconductor, characterized by E -linear behavior due to the line node. In contrast with the s -wave case, there is no clear directional dependence in the spectral evolution in this scale (also see Fig. 6).

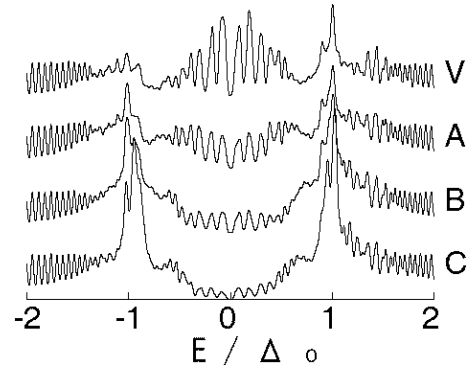


FIG. 4. Local density of states $N(\mathbf{r}, E)$ at $T = 0$ and H_{32} along the NNN direction ($V \rightarrow C$) for the d -wave case. The backside (front) corresponds to V (C)-site defined in Fig. 1. The spectral evolution along the NN direction, which is not shown, shows similar behavior to this figure.

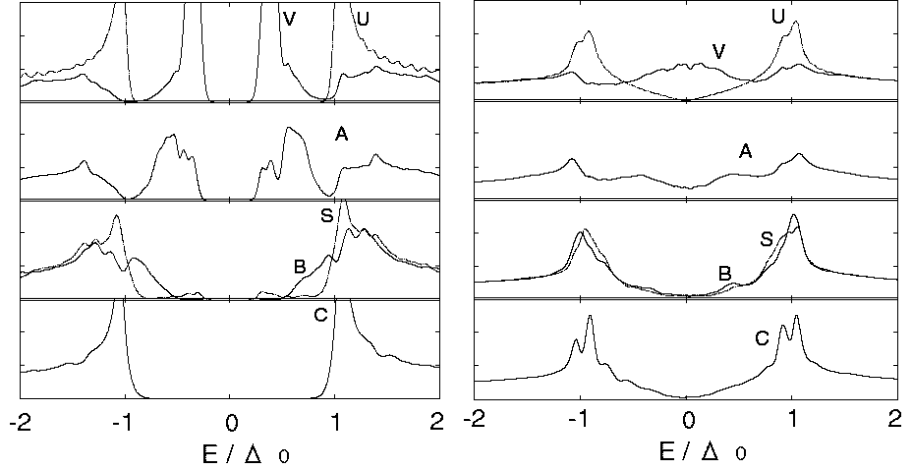


FIG. 5. Local density of states $N(\mathbf{r}, E)$ at $T = 0$ and H_{32} along the NNN direction ($V \rightarrow C$) for the d -wave case. The backside (front) corresponds to V (C)-site defined in Fig. 1. The spectral evolution along the NN direction, which is not shown, shows similar behavior to this figure.

The spectral evolution in a high field H_{12} is depicted for the d -wave case in Fig. 4. The quantum oscillations due to the Landau band quantization becomes evident at a high field. We see rapid oscillations outside the main gap ($|E/\Delta_0| > 1.0$) and slow oscillations inside the main gap ($|E/\Delta_0| < 1.0$). Note that the split features around $E \sim 0$ at the V-site in Fig. 4 is not due to the localized bound state formation. In order to further facilitate the understanding of the T -dependence of the site-dependent $T_1(\mathbf{r})$ behavior, we look into the spectral evolutions for some more details at H_{20} where we calculate $T_1(\mathbf{r})$ in the next section. The LDOS around the vortex for the s -wave case is shown in Fig. 5(a), and the d -wave case is shown in Fig. 5(b). In $N(E, \mathbf{r})$ at the vortex center (the V-site), the gap edge at Δ_0 in the zero-field case (dotted line U) is smeared, and low-energy peaks of the vortex core state appear. In the s -wave case, we see some peaks above the small gap Δ_1 ($\sim \Delta_0^2/E_F$). It is due to the quantization of the energy level in the s -wave case. In the d -wave case, the core state shows zero-energy peak instead of the split peaks in the s -wave case.¹⁵ There is no small gap. The weight of the low-energy states is decreased with going away from the vortex center ($V \rightarrow A \rightarrow B \rightarrow C$). Far from the vortex, $N(E, \mathbf{r})$ is reduced to the DOS of the zero-field case. But, small weight of the low-energy state extending from the vortex core remains there. It is noted that the weight of the low-energy state at the S-site is larger than that of the B-site in the s -wave case, while the S-site is farther from the vortex center [see lines for the S- and B-sites in Fig 5(a)]. It is due to the vortex lattice effect. The quasi-particle transfer between vortices occurs along the line connecting NN vortices (i.e., near

the S-site). This is also seen from Fig. 2(a) indicated by arrows.

To obtain another perspectives of the LDOS image in the d -wave case we plot the spatial distribution of $N(E = 0, \mathbf{r})$ at H_{32} in Fig. 6, which directly relates to the $T_1(\mathbf{r})$ behavior as discussed later. Notice that everywhere $N(E = 0, \mathbf{r}) \neq 0$. The LDOS $N(E = 0, \mathbf{r})$ is largest at the core site and extends towards the NN direction. This shows the characteristic quasi-particle trajectory in the d wave case. The NMR experiment can image this low-energy excitation as is explained later. The detailed expositions of the quasi-particle trajectories in the s -wave^{14,17} and d -wave³⁵ are given previously.

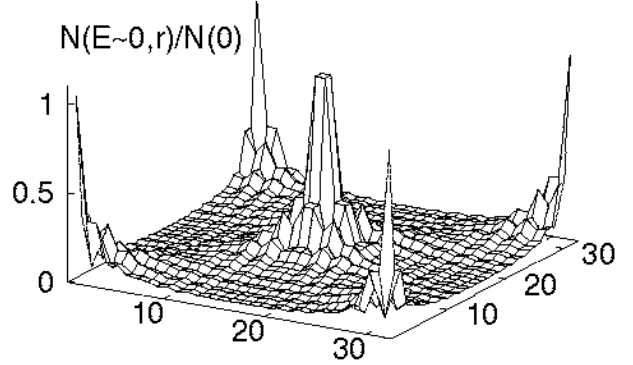


FIG. 6. Topographic view of the local density of states at the Fermi level normalized by the normal state value: $N(E = 0, \mathbf{r})/N(0)$ for the d -wave case at H_{32} . One unit cell (32×32 atomic sites) is shown. The vortices are located at the center and corners of the figure.

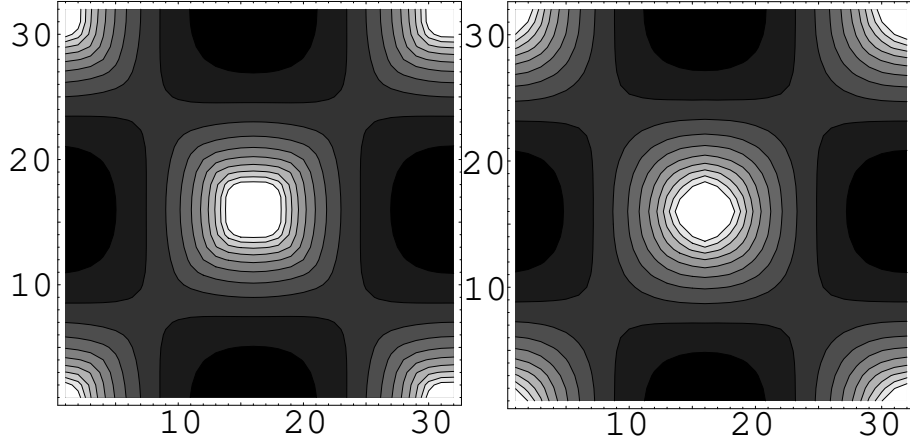


FIG. 7. Topographic view of the local density of states at the Fermi level normalized by the normal state value: $N(E = 0, \mathbf{r})/N(0)$ for the d -wave case at H_{32} . One unit cell (32×32 atomic sites) is shown. The vortices are located at the center and corners of the figure.

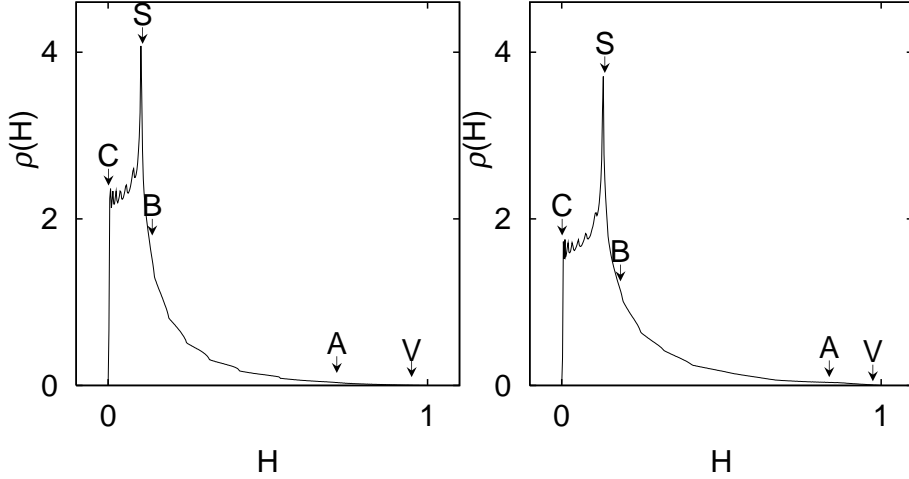


FIG. 8. Histograms $\rho(H)$ of the amplitudes of the magnetic field for the s -wave case (a) and the d -wave case (b). This should correspond to the NMR line shape. The letters in the figures denote the sites defined in Fig. 1.

C. Field distribution in vortex state

In order to determine the one-to-one correspondence between the site and the magnetic field, we calculate the field distributions for the s -wave and d -wave cases. The magnetic field is evaluated via the current distribution through the Maxwell equation:

$$\nabla \times \mathbf{H}(\mathbf{r}) = \frac{4\pi}{c} \mathbf{j}(\mathbf{r}), \quad (30)$$

where the current $\mathbf{j}(\mathbf{r})$ is calculated as

$$j_{\hat{e}}(\mathbf{r}_i) = 2|e|c \text{Im} \left\{ \tilde{t}_{i+\hat{e},i} \sum_{\sigma} \langle \hat{\Psi}_{\sigma}^{\dagger}(\mathbf{r}_{i+\hat{e}}) \hat{\Psi}_{\sigma}(\mathbf{r}_i) \rangle \right\} \quad (31)$$

$$= 2|e|c \text{Im} \left\{ \tilde{t}_{i+\hat{e},i} \sum_{\alpha} [u_{\alpha}^*(\mathbf{r}_{i+\hat{e}}) u_{\alpha}(\mathbf{r}_i) f(E_{\alpha}) + v_{\alpha}(\mathbf{r}_{i+\hat{e}}) v_{\alpha}^*(\mathbf{r}_i) (1 - f(E_{\alpha}))] \right\} \quad (32)$$

for the \hat{e} -direction bond ($\hat{e} = \pm\hat{x}, \pm\hat{y}$) at the site \mathbf{r}_i .

Figures. 7(a) and (b) show the contour plots of the field distributions for one unit cell at H_{32} . It is seen that for the s -wave case the contour plot exhibits rather square-like shape around the core, which is contrasted with a cylindrical shape in the d -wave case. Due to the inter-vortex interaction, the magnetic field around a vortex tends to extend to the NN vortex direction. Then, the field of the s -wave case is modified to a square shape, reflecting the square vortex lattice shape. In the $d_{x^2-y^2}$ -wave case, the magnetic field tends to extend to a axis and b axis directions due to the gap node effect.^{13,34,35} Then, the inter-vortex interaction effect and the gap node effect cancel each other, resulting in a cylindrical shape.

The internal field distributions as a function of the magnetic field, which correspond to the resonance frequency distribution in NMR experiments, are depicted

in Fig. 8. We identify each site (A, B, C, S, and V) in the vortex lattice to these distributions. The one-to-one correspondence between the site position and resonance frequency can be used as a guide for site-selective NMR experiment: Namely, as shown in Figs. 8 (a) and (b), the NMR signal at the maximum cutoff of the resonance spectrum as a function of applied field or probe frequency comes from the vortex core at the V-site. With going away from the center (V→A→B→C), the resonance field is decreased. The signal at the minimum cutoff comes from the C-site. The logarithmic singularity of the resonance field comes from the saddle point of the field at the S-site. Thus it is possible to perform the site-selective $T_1(\mathbf{r})$ measurement by tuning the resonance frequency.

IV. TEMPERATURE DEPENDENCE OF T_1

A. *s*-wave case

We now consider the T -dependence of $T_1(\mathbf{r})$ at each site defined in Fig. 1, which reflects the LDOS discussed above. The *s*-wave case is shown in Fig. 9. We plot $T_1(\mathbf{r})^{-1}$ vs. T for each site in Fig. 9(a), and re-plot it as $\ln T_1(\mathbf{r})$ vs. T^{-1} in Fig. 9(b). We also calculate the zero-field case in our formulation. It is shown as line U in the figures. At the zero field, $T_1 \sim e^{\Delta_0/T}$. Then, the slope of the $\ln T_1$ vs. T^{-1} plot gives the superconducting gap Δ_0 , as the line U in Fig. 9(b). In the presence of vortices, T_1 deviates from the relation $e^{\Delta_0/T}$ at low T due to the low-energy excitation around the vortex core. This deviation was reported in the experiments.⁴ In our results, reflecting the small gap Δ_1 in the *s*-wave case [see Figs. 2(a) and (b), also see the V-site in Figs. 5(a)], T_1 shows the slope Δ_1 at low T in the $\ln T_1$ vs. T^{-1} plot as seen in Fig. 9(b). That is, $T_1 \sim e^{\Delta_1/T}$. With leaving the vortex center, since the amplitude of the low-energy bound states is damped, the weight of $e^{\Delta_1/T}$ gradually decreases. Then the crossover temperature from $e^{\Delta_0/T}$ to $e^{\Delta_1/T}$ is lowered. It is noted that T_1 is faster at the S-site than that of the B-site, while the S-site is further from the vortex center. This non-trivial result is due to the vortex lattice effect noted above [see the foot denoted by arrows in Fig. 2(a)]. We should also notice the behavior of the coherence peak below T_c . As seen in Fig. 9(a),

with approaching the vortex center as C→B, the coherence peak is suppressed. But in the vortex core region (lines V and A), a large new peak grows at intermediate temperatures. This is because the LDOS at the vortex core has peaks at low energy Δ_1 instead of the singularity of DOS at Δ_0 as seen from Figs. 2(a) and (b).

B. *d*-wave case

As for the *d*-wave case, we plot $T_1(\mathbf{r})^{-1}$ vs. T in Fig. 10(a), and re-plot it as a log-log plot in Fig. 10(b). At zero field (line U), we see the power law relation $T_1^{-1} \sim T^3$ of the *d*-wave case as expected. Note that this can be seen only below $T/T_c \simeq 0.1$ in our case. In the presence of vortices, $T_1(\mathbf{r})^{-1}$ deviates from the T^3 -relation, and follows $T_1(\mathbf{r})^{-1} \sim T$ at low temperatures. This deviation was reported in the experiments on high- T_c cuprates.⁵ The origin of the T -linear behavior is the low-energy state around vortices in our case, instead of the residual density of states due to impurities or defects. With approaching the vortex center, the T region of the T -linear behavior is enlarged and it appears from higher temperatures. As seen in Fig. 5(b) of the *d*-wave case, the superconducting gap is buried by the low-energy state around vortices without the small gap of the order Δ_0^2/E_F . Then, $T_1^{-1} \sim T$ at low temperatures in the *d*-wave case instead of the relation $T_1 \sim e^{\Delta_1/T}$ in the *s*-wave case. As seen in Fig. 10, $T_1(\mathbf{r})^{-1}$ at the vortex center (line V) is very large compared with the zero-field case (line U). It reflects the fact that the LDOS of the low-energy state is larger than the DOS of the zero-field case as seen in Fig. 5(b). Figure 6 also shows the LDOS at $E \sim 0$ normalized by $N(0)$: the DOS in the normal state at the Fermi surface. It clearly indicates that the LDOS around the core exceeds the normal state value. This short relaxation may be the evidence of the low-energy peak in the LDOS by the low-energy core state.

The coherence peak below T_c is taken as a manifestation of the *s*-wave symmetry. In the *d*-wave case, the coherence peak is absent. But in the vortex core region, T_1^{-1} has a peak below T_c even in the *d*-wave case. We should be careful not to mistake this peak due to the vortex core relaxation as the usual coherence peak in the NMR experiment when identifying the gap symmetry.

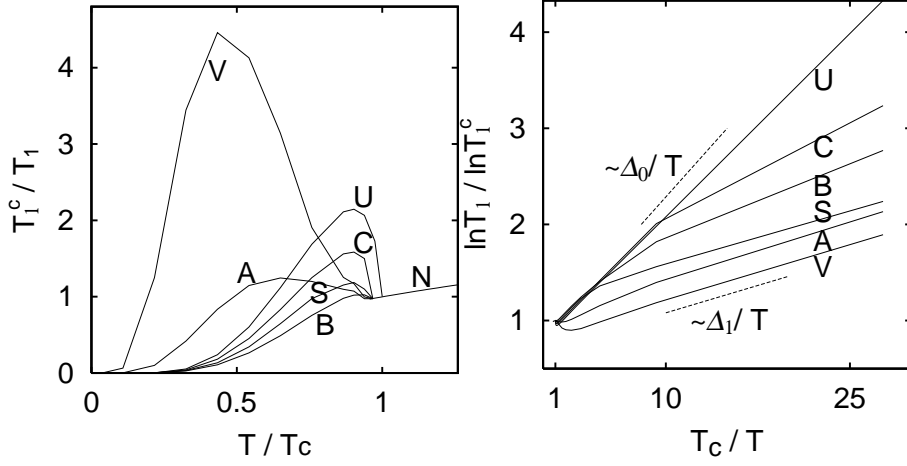


FIG. 9. Temperature dependence of $T_1(\mathbf{r})$ in the s -wave case at the sites V, A, B, C, and S assigned in Fig. 1. (a) $T_1(T_c)/T_1(T)$ is plotted as a function of T/T_c . (b) $\ln T_1(T)/\ln T_1(T_c)$ is plotted as a function of T_c/T . Line U shows the zero field case. The line N is for the normal state at $T > T_c$.

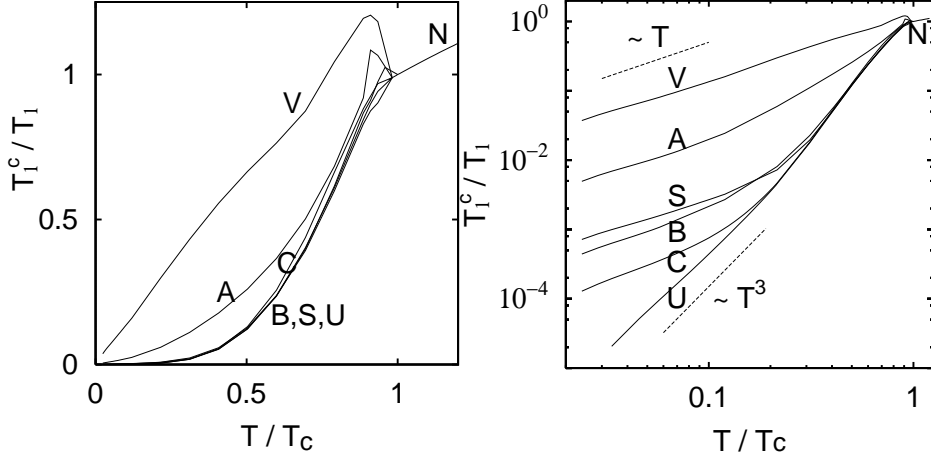


FIG. 10. Temperature dependence of $T_1(\mathbf{r})$ in the d -wave case at the sites V, A, B, C, and S. (a) $T_1(T_c)/T_1(T)$ is plotted as a function of T/T_c . (b) The log-log plot of (a) is shown. Line U shows the zero field case. The line N is for the normal state at $T > T_c$.

V. FIELD DEPENDENCE OF T_1

So far, we only consider $T_1(T)$ under a fixed $H(=H_{20})$, focusing on the T -dependences both in the s -wave and d -wave cases. In this section we investigate the field dependence of the $T_1(T)$ behavior.

A. Field dependence of $T_1(T)$

We calculate the T -dependence of $T_1(T)$ for three representative fields; the weak field H_{32} , the intermediate field H_{20} , and the high field H_{12} in order to see how the coherence peak evolves and the overall T -dependence varies with field. We show the results for the V-site and the S-site (other sites exhibit a similar behavior to the

S-site, thus not shown here). They reflect the field dependence of the LDOS at the vortex core and outside of the core.¹⁵

First, we consider the s -wave case. It is shown in Fig. 12. As seen in Fig. 12(a), the T_1^{-1} -enhancement at the V-site in the intermediate temperature diminishes quickly with increasing field. This is because the sharp low energy peaks of $N(E, \mathbf{r})$ at the vortex core, which is the origin of the enhancement, is smeared by the effect of the quasi-particle transfer between vortices. As shown in Fig. 12(b) for the S-site, the coherence peak below T_c also diminishes with increasing field. In particular, for the high field H_{12} , T_1^{-1} shows a depression below T_c rather than the enhancement. This is caused by the smearing of the superconducting gap by the low energy state around the vortex, which extends outside of the core region by the quasi-particle transfer between vortices. With increas-

ing field, the singularity of the LDOS at the bulk gap edge $E=\Delta_0$ is smeared. Then the coherence peak diminishes. It is qualitatively consistent to the observation on V_3Sn .⁴²

The similar field-dependence of T_1 occurs in the d -wave case. The T -dependence of T_1^{-1} is shown in Fig. 13. At the V-site [Fig. 13(a)], the enhancement of T_1^{-1} is depressed as H increases. It reflects that the low energy peak of the LDOS around the vortex is smeared by the quasi-particle transfer between vortices. At the S-site [Fig. 13(b)], T_1^{-1} below T_c is suppressed as H increases. It reflects that the low energy state around the vortex smears the d -wave superconducting gap-edge. The log-log plots of T_1^{-1} vs. T are presented in Fig. 13 to see the low temperature behavior. At the V-site [Fig. 13(a)], the T -linear coefficient in $T_1^{-1}(T)$ is depressed with increasing H at low temperature. This is because the inter-vortex quasi-particle transfer smears the low energy

quasi-particle peak of the LDOS at the vortex core. At the S-site [Fig. 13(b)], $T_1^{-1}(T)$ is increased with raising H at low temperatures, while $T_1^{-1}(T)$ is decreased with raising H near T_c [Fig. 13(b)]. Because the vortex contribution is increased and the amplitude of the low energy state extending outside the vortex core becomes large, the relaxation time at low temperatures becomes short with increasing external magnetic field. This tendency coincides qualitatively with the observation of high- T_c cuprates by Ishida *et al.*⁵ or an organic superconductor κ -(ET)₂Cu[N(CN)₂]Br by Mayaffre *et al.*⁴³

We note that the quantum oscillations due to the Landau band quantization affects the low temperature behavior of T_1 at extreme high fields. In Fig. 13, $T_1^{-1}(T)$ at the high field H_{12} deviates from the T -linear behavior. It deviates downward (upward), when the LDOS is minimum (maximum) at the Fermi energy in the quantum oscillation of the LDOS (Fig. 4).

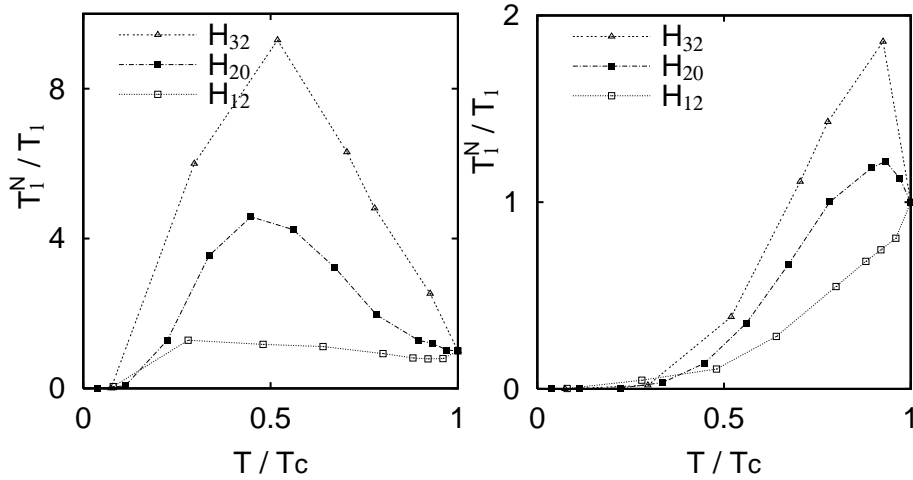


FIG. 11. $T_1(T_c)/T_1(T)$ is plotted as a function of T/T_c for the s -wave case at H_{32} , H_{20} , and H_{12} . T_c and $T_1(T_c)$ are defined by each H . (a) the V-site and (b) the S-site.

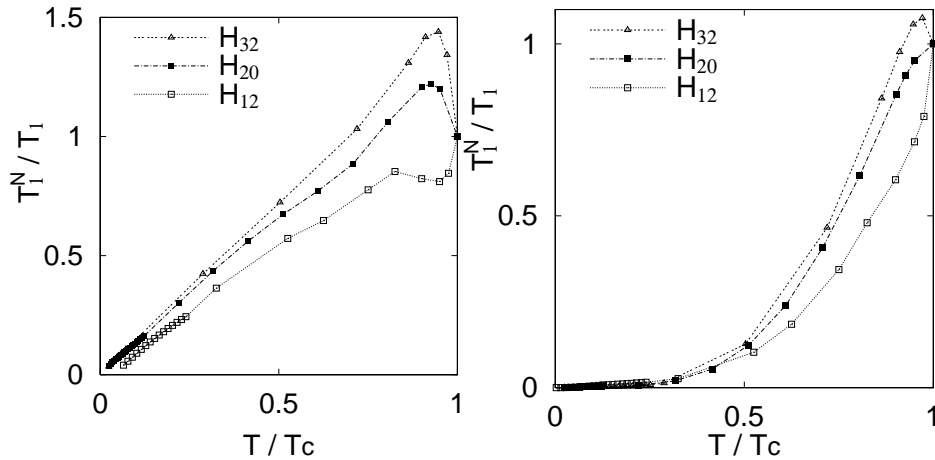


FIG. 12. $T_1(T_c)/T_1(T)$ is plotted as a function of T/T_c for the s -wave case at H_{32} , H_{20} , and H_{12} . T_c and $T_1(T_c)$ are defined by each H . (a) the V-site and (b) the S-site.

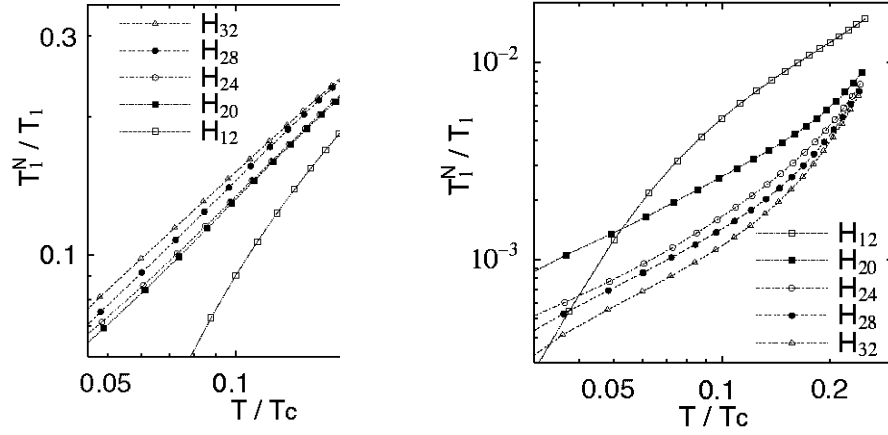


FIG. 13. The low temperature behavior of $T_1(T)^{-1}$. The log-log plots of $T_1(T_c)/T_1(T)$ vs. T/T_c are presented for the d -wave case at H_{32} , H_{28} , H_{24} , H_{20} and the high field H_{12} . T_c and $T_1(T_c)$ are defined by each H . (a) the V-site and (b) the S-site.

B. $T_1(\mathbf{r}, T)$ vs. LDOS

Here we investigate the relationship between $T_1^{-1}(\mathbf{r})$ at low temperatures and the low energy excitations $N(E=0, \mathbf{r})$ in the d -wave case. In the low temperature region, T_1^{-1} shows T -linear behavior. First, we plot the spatial distribution of $T_1^{-1}(\mathbf{r}, T \sim 0)$ at H_{32} for a unit cell in Fig. 14. This shows that $T_1^{-1}(\mathbf{r}, T \sim 0)$ normalized by the normal state value T_1^N is largest at the core and exceeds its normal state value. Namely, with approaching the vortex core, T_1^{-1} increases. This tendency is in qualitative agreement with a measurement by Milling and Slichter²⁷ on ^{63}Cu NMR experiment of YBCO.

The histogram $\rho(T_1^{-1})$ of $T_1^{-1}(\mathbf{r}, T \sim 0)$ is shown in Fig. 15, where the values of $T_1^{-1}(\mathbf{r}, T \sim 0)$ for the total 32×32 sites is classified according to its magnitudes. This indicates that the vast majority sites outside the vortex core exhibit long relaxation times, but certain few sites around the vortex core exhibit short relaxation time, which contains useful information on the site-dependent low energy excitations associated with the vortex.

This topography of $T_1^{-1}(\mathbf{r}, T \sim 0)$ in Fig. 14 looks similar to that of LDOS $N(E=0, \mathbf{r})$ in Fig. 6. In fact, as shown in Fig. 16 where $T_1^{-1}(\mathbf{r}, T \sim 0)$ vs. $N^2(E=0, \mathbf{r})/N^2(0)$ is plotted, the linear relationship between them is apparently seen. It implies that $T_1^{-1}(\mathbf{r}, T \sim 0)$ at low T is governed by the low energy excitations at each site. Then, the site-selective $T_1^{-1}(\mathbf{r}, T \sim 0)$ is a good measure of the local core excitations. The LDOS around the vortex core can be estimated quantitatively from the slope of $T_1^{-1}(\mathbf{r})$ at low T .

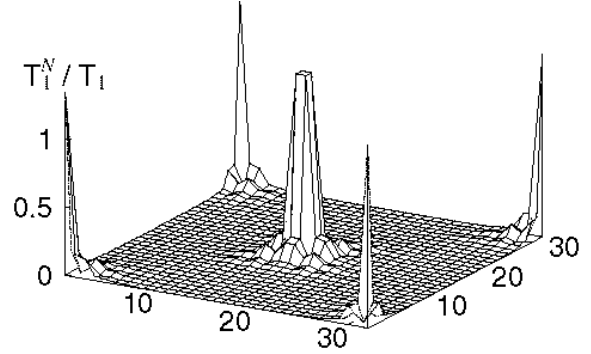


FIG. 14. Topographic view of the site-dependent relaxation time $T_1^N/T_1(\mathbf{r})$ for the d -wave case at H_{32} and $T \sim 0$. It is normalized by its normal state value T_1^N . One unit cell (32×32 atomic sites) is shown. The vortices are located at the center and corners of the figure.

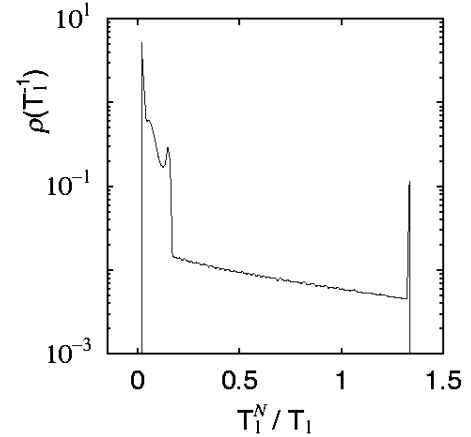


FIG. 15. Histogram $\rho(T_1^{-1})$ of T_1^{-1} corresponding to Fig. 14.

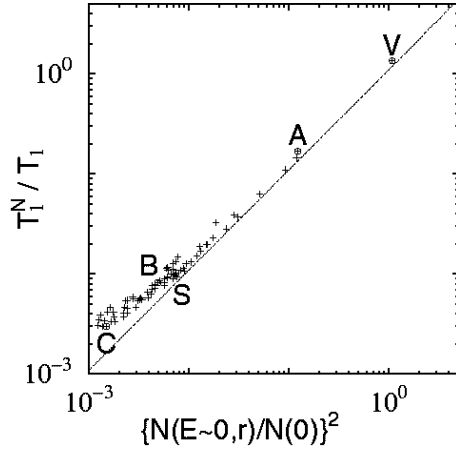


FIG. 16. The linear relationship between $T_1^N/T_1(\mathbf{r})$ and $[N(E=0, \mathbf{r})/N(0)]^2$. We plot the 32×32 lattice point values of the normalized $T_1^N/T_1(\mathbf{r})$ shown in Fig. 14 and the square of the normalized LDOS $N(E=0, \mathbf{r})/N(0)$ shown in Fig. 6. The letters in the figures denote the sites defined in Fig. 1. The dotted line shows the linear relation $T_1^N/T_1(\mathbf{r}) \propto [N(E=0, \mathbf{r})/N(0)]^2$.

VI. CONCLUSION AND DISCUSSIONS

We have calculated the nuclear relaxation time T_1 in mixed state in the microscopic framework of the BdG theory and demonstrated that the site-selective T_1 is a good probe to extract detailed information on low lying vortex core excitations. We have investigated the site-dependence, T -dependence and field-dependence of T_1 both for the s -wave and d -wave superconductors.

Traditionally, the vortex contribution was considered as the spin diffusion to the normal region of the vortex core,^{5,9} and T_1 is treated as the spatial average. However, we can investigate the position dependence of $T_1(\mathbf{r})$ around vortices through the resonance field dependence. This is an advantage of NMR over other methods. We should clarify the local mechanism of the relaxation (i.e., whether the relaxation occurs locally, or it is averaged by the spin diffusion). It is noted that in the clean limit the vortex core region is not a simple core filled by normal state electrons.^{1,10–14,17,34–37} There, the characteristic T -dependence is expected near the vortex core other than a simple T -linear behavior, reflecting the rich structure of the low energy state around the vortex core.

We expect that the NMR imaging study just explained here will provide vital information for the vortex core state in high- T_c cuprates. As for the problem whether the quantization of the energy levels occurs or not, $T_1 \sim e^{\Delta_1/T}$ if the gap Δ_1 ($\sim \Delta_0^2/E_F$) is present in the excitation due to the quantization. If this small gap is absent, $T_1^{-1} \sim T$. As for the problem whether the zero-energy peak exists or not in the core state, the relaxation at the core becomes eminently faster than that of the zero-field case (or that far from the vortex) at low temperature, if the zero-energy peak exists in the

LDOS as suggested in the theoretical study. If the peak structure is absent within Δ_0 as reported in the STM experiments on BSCCO, the relaxation is slow even at the vortex core as in the zero-field superconducting case.

We have pointed out a pitfall of the conventional procedure of the NMR experiment to extract the nodal gap structure by analyzing the power law of the T -dependence of T_1 or the coherence peak. Even in the d -wave pairing, T_1^{-1} shows enhancement below T_c by the vortex core contribution.

Finally, we stress that, to perform an idealized site-selective NMR measurement, we need a clear NMR resonance line shape of the vortex lattice as shown in Fig. 8 or as that obtained by a beautiful experiment on vanadium.^{6,7} In the resonance line shape, the signal near the upper (lower) cutoff of the field distribution gives the information from the vortex core (the outside of the core). However, even in the case when the resonance line shape of the vortex lattice is not clear, if we analyze the fast and slow relaxation processes separately, the fast relaxation process includes the information of the vortex core contribution.⁴⁴ We hope that future NMR experiments confirm our proposal of the site-selective NMR, and clarify the relation of $T_1(\mathbf{r})$ and $N(E, \mathbf{r})$. If this experimental method is established, it can be a powerful method to investigate the exotic mechanism of the unconventional superconductors by spatially imaging the low energy quasi-particle excitation around the vortex cores.

APPENDIX A:

The equation of motion for the Green function in a 2×2 matrix form is written in the coordinate space as

$$\sum_{\mathbf{x}''} \left\{ -\hbar \frac{\partial}{\partial \tau} \mathbf{1} \delta(\mathbf{x} - \mathbf{x}'') - \begin{pmatrix} K(\mathbf{x}, \mathbf{x}'') & \Delta(\mathbf{x}, \mathbf{x}'') \\ \Delta^\dagger(\mathbf{x}, \mathbf{x}'') & -K^*(\mathbf{x}, \mathbf{x}'') \end{pmatrix} \right\} \hat{g}(\mathbf{x}'' \tau, \mathbf{x}' \tau') = \hbar \delta(\mathbf{x} - \mathbf{x}') \delta(\tau - \tau') \mathbf{1} \quad (\text{A1})$$

where $\mathbf{1}$ is the 2×2 unit matrix. We put the completeness relation:

$$\delta(\mathbf{x} - \mathbf{x}') \mathbf{1} = \sum_{E_\alpha > 0} \begin{pmatrix} u_\alpha(\mathbf{x}) & -v_\alpha^*(\mathbf{x}) \\ v_\alpha(\mathbf{x}) & u_\alpha^*(\mathbf{x}) \end{pmatrix} \begin{pmatrix} u_\alpha^*(\mathbf{x}') & v_\alpha^*(\mathbf{x}') \\ -v_\alpha(\mathbf{x}') & u_\alpha(\mathbf{x}') \end{pmatrix} \quad (\text{A2})$$

before $\hat{g}(\mathbf{x}'' \tau, \mathbf{x}' \tau')$ in Eq. (A1), and use the BdG equation of the form

$$\sum_{\mathbf{x}'} \begin{pmatrix} K(\mathbf{x}, \mathbf{x}') & \Delta(\mathbf{x}, \mathbf{x}') \\ \Delta^\dagger(\mathbf{x}, \mathbf{x}') & -K^*(\mathbf{x}, \mathbf{x}') \end{pmatrix} \begin{pmatrix} u_\alpha(\mathbf{x}') & -v_\alpha^*(\mathbf{x}') \\ v_\alpha(\mathbf{x}') & u_\alpha^*(\mathbf{x}') \end{pmatrix} = \begin{pmatrix} u_\alpha(\mathbf{x}) & -v_\alpha^*(\mathbf{x}) \\ v_\alpha(\mathbf{x}) & u_\alpha^*(\mathbf{x}) \end{pmatrix} \begin{pmatrix} E_\alpha & 0 \\ 0 & -E_\alpha \end{pmatrix} \quad (\text{A3})$$

for $E_\alpha > 0$. After the Fourier transformation of τ to ω_n , the inversion of the matrix product leads to

$$\hat{g}(\mathbf{x}, \mathbf{x}', \omega_n) = \sum_{E_\alpha > 0} \begin{pmatrix} u_\alpha(\mathbf{x}) & -v_\alpha^*(\mathbf{x}) \\ v_\alpha(\mathbf{x}) & u_\alpha^*(\mathbf{x}) \end{pmatrix} \begin{pmatrix} \frac{1}{i\omega_n - E_\alpha/\hbar} & 0 \\ 0 & \frac{1}{i\omega_n + E_\alpha/\hbar} \end{pmatrix} \begin{pmatrix} u_\alpha^*(\mathbf{x}') & v_\alpha^*(\mathbf{x}') \\ -v_\alpha(\mathbf{x}') & u_\alpha(\mathbf{x}') \end{pmatrix} \quad (\text{A4})$$

with the help of the completeness and the orthogonal relation of the wave functions. In the term with $(i\omega_n + E_\alpha/\hbar)^{-1}$, we use the symmetry property: $u_\alpha \rightarrow -v_\alpha^*$, $v_\alpha \rightarrow u_\alpha^*$ when $E_\alpha \rightarrow -E_\alpha$. Then, Eqs. (20)-(23) are obtained.

APPENDIX B:

The spin-spin correlation function is defined as

$$\chi_{-,+}(x, x') = \langle T_\tau [S_-(x) S_+(x')] \rangle = \left\langle T_\tau [\psi_\downarrow^\dagger(x) \psi_\uparrow(x) \psi_\uparrow^\dagger(x') \psi_\downarrow(x')] \right\rangle \quad (\text{B1})$$

with $x \equiv (\mathbf{x}, \tau)$. This can be rewritten in terms of the thermal Green functions,

$$\chi_{-,+}(x, x') = g_{11}(x, x') g_{22}(x, x') - g_{12}(x, x') g_{21}(x, x'). \quad (\text{B2})$$

After the Fourier transformation of τ , we obtain

$$\chi_{-,+}(\mathbf{x}, \mathbf{x}', \Omega_n) = T \sum_{\omega_n} \{ g_{11}(\mathbf{x}, \mathbf{x}', \omega_n) g_{22}(\mathbf{x}, \mathbf{x}', \Omega_n - \omega_n) - g_{12}(\mathbf{x}, \mathbf{x}', \omega_n) g_{21}(\mathbf{x}, \mathbf{x}', \Omega_n - \omega_n) \}. \quad (\text{B3})$$

Then, substituting Eqs. (20)-(23) and performing ω_n -sum, the spin-spin correlation function with real frequency Ω is reduced to

$$\chi_{-,+}(\mathbf{x}, \mathbf{x}', i\Omega_n \rightarrow \Omega + i\eta) = - \sum_{\alpha, \beta} u_\alpha(\mathbf{x}) u_\beta^*(\mathbf{x}) \{ u_\alpha^*(\mathbf{x}') u_\beta(\mathbf{x}') + v_\alpha^*(\mathbf{x}') v_\beta(\mathbf{x}') \} \frac{f(E_\alpha) - f(E_\beta)}{E_\alpha - E_\beta - \Omega - i\eta}. \quad (\text{B4})$$

Here, we used the symmetry property: $u_\alpha \rightarrow -v_\alpha^*$, $v_\alpha \rightarrow u_\alpha^*$ when $E_\alpha \rightarrow -E_\alpha$.

-
- ¹ For review: K. Machida, M. Ichioka, N. Hayashi, and T. Isoshima, in *The Superconducting State in Magnetic Fields*, edited by C.A.R. Sá de Melo, (World Scientific, Singapore, 1998), Chap. 13.
- ² J. Sonier, J. H. Brewer, and R. F. Kiefl, preprint (submitted to Rev. Mod. Phys.).
- ³ See for example, recent technical developments: J. Haase, N.J. Curro, R. Stern, and C.P. Slichter, Phys. Rev. Lett. **81**, 1489 (1998). K.R. Gorny, O.M. Vyaselev, S. Yu, C.H. Pennington, W.L. Hults, and J.L. Smith, Phys. Rev. Lett. **81**, 2340 (1998).
- ⁴ B.G. Silbernagel, M. Weger, and J.E. Wernick, Phys. Rev. Lett. **17**, 384 (1966).
- ⁵ K. Ishida, Y. Kitaoka, and K. Asayama, Solid State Commun. **90**, 563 (1994). K. Ishida, Y. Kitaoka, K. Asayama, K. Kadowaki, and T. Mochiku, J. Phys. Soc. Jpn. **63**, 1104 (1994).
- ⁶ W. Fite II, and A.G. Redfield, Phys. Rev. Lett. **17**, 381 (1966).
- ⁷ A. Kung, Phys. Rev. Lett. **25**, 1006 (1970).
- ⁸ C. Caroli, P.-G. de Gennes, and J. Matricon, Phys. Lett. **9**, 307 (1964).
- ⁹ C. Caroli, and J. Matricon, Phys. Kondens. Mater. **3**, 380 (1965).
- ¹⁰ N. Hayashi, T. Isoshima, M. Ichioka, and K. Machida, Phys. Rev. Lett. **80**, 2921 (1998).
- ¹¹ N. Hayashi, M. Ichioka, and K. Machida, J. Phys. Soc. Jpn., **67**, 3368 (1998).
- ¹² G. E. Volovik, JETP Lett. **58**, 469 (1993).
- ¹³ M. Ichioka, A. Hasegawa, and K. Machida, Phys. Rev. B **59**, 184, and 8902 (1999).
- ¹⁴ N. Hayashi, M. Ichioka, and K. Machida, Phys. Rev. Lett. **77**, 4074 (1996).
- ¹⁵ Y. Wang, and A.H. MacDonald, Phys. Rev. B **52**, 3876 (1995).
- ¹⁶ M. Franz, and Z. Tešanović, Phys. Rev. Lett. **80**, 4763 (1998).
- ¹⁷ M. Ichioka, N. Hayashi, and K. Machida, Phys. Rev. B **55**, 6565 (1997).
- ¹⁸ Y. Wang, and A.H. MacDonald, Solid State Commun. **109**, 289 (1998). W.A. Atkinson, and A.H. MacDonald, Phys. Rev. B **60**, 9295 (1999).
- ¹⁹ B. Jankó, and J.D. Shore, Phys. Rev. B **46**, 9270 (1992).
- ²⁰ A.S. Mal'nikov, J. Phys. Cond. Matt. **21**, 4219 (1999).
- ²¹ B. Jankó, Phys. Rev. Lett. **82**, 4703 (1999).
- ²² M. Franz, and Z. Tešanović, preprint (con-mat/9903152).
- ²³ I. Maggio-Aprile, Ch. Renner, A. Erb, E. Walker, and Ø. Fischer, Phys. Rev. Lett. **75**, 2754 (1995); J. Low Temp. Phys. **105**, 1129 (1996).
- ²⁴ E.W. Hudson, S.H. Pan, A.K. Gupta, K.-W. Ng, and J.C. Davis, Science **285**, 88 (1999).
- ²⁵ Ch. Renner, B. Revaz, K. Kadowaki, I. Maggio-Aprile, and Ø. Fischer, Phys. Rev. Lett. **80**, 3606 (1998).
- ²⁶ N.J. Curro, C.P. Slichter, W.C. Lee, and D.M. Ginsberg, A.P.S. March Meeting Abstract (1999).
- ²⁷ C. Milling, and C.P. Slichter, preliminary results referred to by Morr and Wortis²⁹.
- ²⁸ R.Wortis, A.J. Berlinsky, and C. Kallin, preprint (cond-mat/9907093).
- ²⁹ D.K. Morr, and R.Wortis, preprint (cond-mat/9907192).
- ³⁰ M. Horvatić, private communication.
- ³¹ R. Leadon, and H. Suhl, Phys. Rev. **165**, 596 (1968).
- ³² A brief report of this work: M. Takigawa, M. Ichioka, and K. Machida, Phys. Rev. Lett. **83**, 3057 (1999).
- ³³ P.G. de Gennes, *Superconductivity in Metals and Alloys* (W.A. Benjamin, New York, 1966).
- ³⁴ M. Ichioka, N. Hayashi, N. Enomoto, and K. Machida, J. Phys. Soc. Jpn. **64**, 4547 (1995).
- ³⁵ M. Ichioka, N. Hayashi, N. Enomoto, and K. Machida, Phys. Rev. B **53**, 15316 (1996).
- ³⁶ N. Hayashi, M. Ichioka, and K. Machida, Phys. Rev. B **56**, 9052 (1997).
- ³⁷ M. Ichioka, A. Hasegawa, and K. Machida, J. Superconductivity **12**, 571 (1999).
- ³⁸ L. Kramer, and W. Pesch, Z. Phys. **269**, 59 (1974). W. Pesch, and L. Kramer, J. Low Temp. Phys. **15**, 367 (1974).
- ³⁹ *The Superconducting State in Magnetic Fields*, edited by C.A.R. Sá de Melo, (World Scientific, Singapore, 1998), Chaps. 7 and 8.
- ⁴⁰ H. Won, and K. Maki, Phys. Rev. B **53**, 5927 (1996).
- ⁴¹ Our definition gives the same phase factor as that of M. Ozaki, Y. Hori, and A. Goto, Prog. Theor. Phys. **101**, 769 (1999).
- ⁴² Y. Masuda and N. Okubo, J. Phys. Soc. Jpn. **26**, 309 (1969).
- ⁴³ H. Mayaffre, P. Wzietek, D. Jérôme, C. Lenoir, and P. Batail, Phys. Rev. Lett. **75**, 4122 (1995).
- ⁴⁴ H. Mukuda, private communication.